Laser and Particle Beams

cambridge.org/lpb

Transport of intense beams with current-dependent initial conditions in linearly tapered solenoid channels

J. R. Harris

Air Force Research Laboratory, Albuquerque, NM 87117, USA

Research Article

Cite this article: Harris JR (2019). Transport of intense beams with current-dependent initial conditions in linearly tapered solenoid channels. *Laser and Particle Beams* **37**, 312–323. https://doi.org/10.1017/S0263034619000612

Received: 30 July 2019
Revised: 7 August 2019
Accepted: 19 August 2019
First published online: 21 October 2019

Key words:
beam focusing; electron beam; intense beams; Space charge

Author for correspondence: J. R. Harris, Kirtland Air Force Base, 3550 Aberdeen Ave. SE, Albuquerque, NM 87117, USA.

Abstract

In electron beams where space charge plays an important role in the beam transport, the beams' transverse and longitudinal properties will become coupled. One example of this is the transverse–longitudinal correlation produced in a current-modulated beam generated in a DC electron gun, formed through the competition between the time-dependent radial space charge force and the time-independent radial focusing force. This correlation will cause both the slice radius and divergence of the beam extracted from the gun to depend on the slice current. Here we consider the transport of such a beam in a linearly tapered solenoid focusing channel. Transport performance was generally improved with longer taper lengths, minimal initial correlation between slice divergence and slice current, and moderate degrees of initial correlation between initial slice radius and slice current. Performance was also generally improved with lower slice emittances, although surprisingly transport was improved by slightly increasing the assumed slice emittance in certain limited circumstances.

Introduction

In many beams, the impact of space charge must be taken into account. One of the important consequences of this is that the beam's transverse and longitudinal dynamics become coupled, which can happen in a number of ways (Reiser, 2008). For example, space charge exerts both transverse and longitudinal forces which push charge from regions of higher concentration to regions of lower concentration. In the transverse direction, this causes radial beam expansion, which is generally opposed by transverse focusing, while in the longitudinal direction this can cause beam lengthening, generation of space charge waves, and changes in the beam frequency content (Harris et al., 2007*b*; Hoff *et al.*, 2017). Since beam current is a function of longitudinal position along the beam due to temporal structure imposed on the beam current pulse either deliberately (Li and Lewellen, 2008; Poursaleh, 2013) or as a natural result of time-varying fields in the beam source (Mohsen et al., 2018), the strength of space charge-driven effects will also vary along its length. Changes in beam radius affect the propagation of longitudinal space charge waves (Harris et al., 2007*a*; Reiser, 2008), while the propagation and interference of those longitudinal space charge waves can drive changes in beam current leading to transverse effects such as mismatch oscillations and halo formation (Harris et al., 2007*b*; Poole *et al.*, 2009), potentially leading to beam loss.

A complete treatment of a beam's dynamics when space charge is important therefore requires full coupling of the transverse and longitudinal beam dynamics. However, the longitudinal evolution of space charge-dominated beams generally occurs much more slowly than their transverse evolution, allowing the longitudinal variation in current along a beam pulse to be initially approximated as fixed, while the transverse evolution of each slice of the beam will depend on its initial conditions, the current in that slice, and the nature of the transverse focusing. In doing this, we consider the impact of the longitudinal current variation in the transverse dynamics, but not the impact of the transverse dynamics on the longitudinal current variation.

We have previously used this approach to consider several aspects of space charge-dominated electron beam transport, with the transverse dynamics calculated using the transverse envelope equation (Reiser, 2008). However, to do this correctly, the correlation between the beam's transverse initial conditions (radius and divergence) and the beam current must be taken into account. This correlation arises through a competition between the time-dependent radial space charge force and the time-independent radial focusing force in the gun. Numerical simulations of DC electron guns indicated that the initial radius and divergence of such a beam could be approximated as linear functions of the slice current, provided that the longitudinal variation in beam current was slower than the transit time across the gun (Harris et al., 2012). The transport of these beams through transverse focusing channels of varying types was then considered. In Harris *et al.* (2013), beams launched with the initial conditions found through

CAMBRIDGE UNIVERSITY PRESS

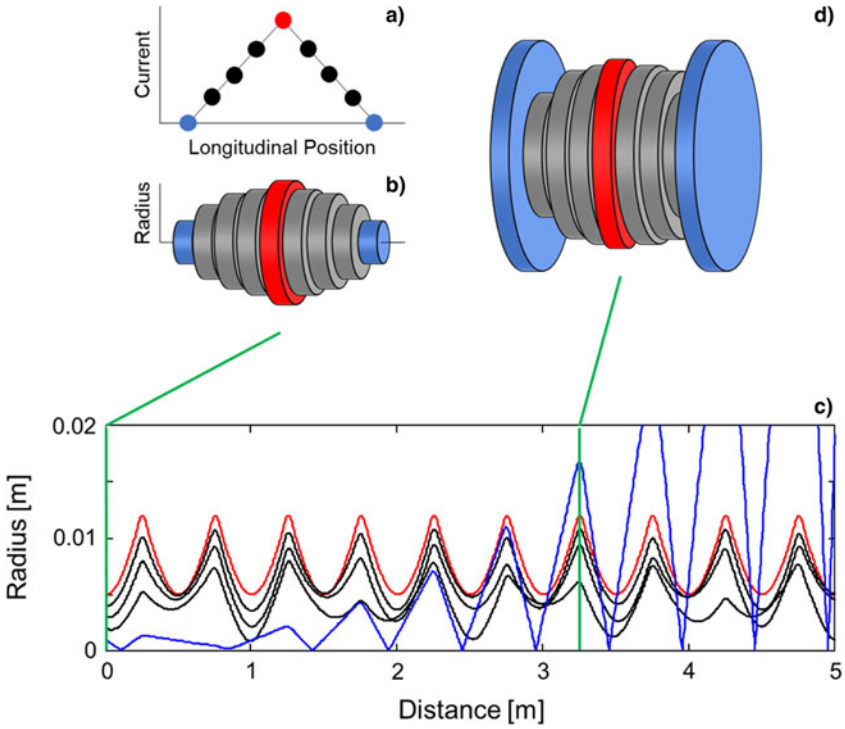

Fig. 1. Initial transverse–longitudinal correlations and well-confined beams. (a) An electron beam is generated with a current which varies along its length, from "zero current" at the beam ends (blue) to a peak current somewhere between those ends (red). (b) The competition between transverse space charge and focusing forces in the gun introduces a correlation between the radius, divergence, and current in each slice of the beam. (c) With longitudinal evolution in the beam neglected, each slice of the beam independently evolves in radius and divergence as it propagates along the transport channel [here, a thin-lens periodic solenoid channel rather than the uniform focusing channel of Harris *et al.* (2013)]. (d) In this case, the "zero current" slice is strongly mismatched to the channel, so that its radius eventually exceeds that of the peak-current slice. The "zero current" slice, and therefore the overall beam, are considered "not well-confined," while the remaining slices are all "well-confined."

simulation in Harris *et al.* (2012) were injected through a matching solenoid into a uniform solenoid focusing channel. We configured the channels for matched transport of the peak current slice and considered the remaining slices to be "well confined" if their radii were less than or equal to the radius of the peak current slice at all locations along the transport channel (Fig. 1). It was found that the range of matching solenoid locations for which well-confined transport could be found depended strongly on the nature of the initial transverse–longitudinal correlation.

The use of "well-confined" beams as a metric is intended to flag any mismatch oscillations or transport instabilities that are large enough to be of concern for beam loss in a system designed for the transport of the peak current slice, without needing to actually specify a particular beam pipe size. The results of such beam loss would be similar to the introduction of apertures (Ein-Gal, 2009; Stancari et al., 2011), which can lead to unwanted radiation production (Peterson, 2011), changes in the transverse density profile of a beam (Bernal et al., 1999a; 2002), and alterations in the nature of the transverse–longitudinal correlation on the beam (Harris and Lewellen, 2010a; 2010b). However, slowly growing instabilities may not be flagged by this approach if the radius of the reduced-current slice does not exceed that of the peak current slice except at distances much longer than considered in the calculation. In these situations, though, the long path length necessary for the slice to become not well confined according to this calculation likely requires the longitudinal evolution of the beam to be taken into consideration, thus violating a fundamental assumption of the calculation.

In Harris et al. (2017), we attempted to further generalize this study. The linear dependence of initial slice radius and the divergence on slice current was retained, but the coefficients of that dependence were treated as free parameters, constrained only by the assumption that the peak current slice was emitted at the channel design radius and with zero initial divergence [i.e., the beam was assumed to be launched from an idealized Pierce gun (Pierce, 1940)]. No matching section was used, and instead, the beam was directly injected into a uniform or periodic solenoid channel, with the channel strength adjusted for matched transport of the peak current slice. Consistent with Harris *et al.* (2013), it was found that the correct choice of initial transverse–longitudinal correlation greatly improved transport through the channels, with the preferred configurations having a relatively strong correlation between the initial slice radius and slice current, but minimal correlation between the initial slice divergence and slice current. Transport was also improved with decreasing gap length between solenoid lenses, consistent with observations in Bernal *et al.* (2006), that a higher fill factor of focusing elements in a transport channel enabled transport of beams with a wider range of initial conditions.

A key question remaining from that work was, to what extent does the insight gained from studying that particular transport channel configuration apply to other transport channel configurations? Were these general results, or were they a result of the specific channel type used in that paper? To test this, it is necessary to repeat the same general calculation, but with a significantly different channel configuration.

The observation of Bernal *et al.* (2006), taken to its extreme, suggests the use of a continuous focusing channel, such as that formed by a long solenoid. However, these channels are not generally convenient for changing the beam size. In periodic focusing channels, this is often done by focusing the beam through a waist and then using a second focusing element to check its divergence when it has reached the desired radius; note that in intense beams with time-varying current, this can only be done for a single slice of the beam. The closest analog in a continuous focusing channel would involve a longitudinal taper in the channel focusing strength. Axially tapered magnetic fields of this type are used in some electron-beam devices, including micro- and millimeter wave sources (Leupold et al., 1992), and in certain flat-beam electron source concepts (Brinkmann et al., 2001; Efthymiopoulos

https://doi.org/10.1017/S0263034619000612 Published online by Cambridge University Press

et al., 2013; Floettmann, 2004; James et al., 1991; Leupold, 1987; 1993; Leupold et al., 1992; McDonald et al., 2014; Sayed and Berg, 2014).

Our present objective is therefore to extend Harris et al. (2017*b*) by considering the case of transport in continuous solenoidal focusing channels where the channel strength varies over its length. Channels with a linear taper in focusing strength are considered, as are the effects of changes in slice emittance. Performance was generally improved with longer taper lengths, minimal initial correlation between slice divergence and slice current, and moderate degrees of initial correlation between initial slice radius and slice current. Performance was also generally improved with lower slice emittances, with the dependence on slice emittance being largest for long, strong tapers, and with transverse–longitudinal correlation strengths which generally optimized beam transport. Under very limited conditions, transport was found to be improved by slightly larger values of slice emittance than the standard 1 μm value used here.

Approach

Envelope calculations and initial conditions

Our approach will be similar to that used in Harris et al. (2017*b*) but altered to reduce calculation time and simplify the presentation of the results. The initial slice radius and divergence will be assumed to depend on the slice current according to

$$r(I) = R + a_1(I - I_{\max}) \tag{1}$$

$$r'(I) = b_1(I - I_{\max}), \tag{2}$$

with the linearity coefficients a_1 and b_1 defining the strength and nature of the correlation (Fig. 2). These initial conditions incorporate the assumption that the electron gun produces a beam with radius R and zero divergence for the peak current slice (current $I_{\max}$). The value of R and the initial strength of the focusing channel will be chosen so that the peak current slice will be matched to the channel when the channel strength is not tapered ($C = 1$). Beam transport in the channel is calculated using the envelope equation (Reiser, 2008)

$$r'' + k_0^2 r - \frac{K}{r} - \frac{\varepsilon^2}{r^3} = 0 \tag{3}$$

Here $r(z)$ is the slice radius, primes denote differentiation with respect to the direction of travel of the beam (z), $k_0 = |qB(z)|/2mc\beta\gamma$ defines the strength of the applied focusing produced by the axial magnetic field $B(z)$, $K = 2I/I_0\gamma^3\beta^3$ is the generalized perveance, I_0 is 17 kA for electrons, ε is the unnormalized slice emittance, m and q are the mass and charge of the electron, and γ and β are the relativistic parameters. The beam is assumed to be generated with zero canonical angular momentum. Following Harris *et al.* (2017*b*), a slice emittance of 1 μm was used in most cases, although it turned out that in a small number of cases, this was not sufficient to ensure proper treatment of the zero current slices at waists in these calculations; with zero space charge, waist formation is determined by the emittance term in Eq. (3), and emittance values that are too small may lead to very small waist radii which are not handled correctly in MathCad for the step size

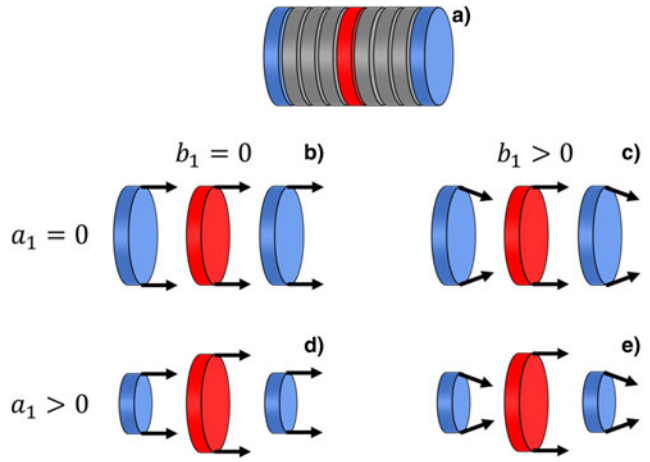

Fig. 2. Relationship of slice initial conditions to the parameters a_1 and b_1. (a) A current-modulated beam consists of multiple slices, each of which is thin enough to be approximated as having a single current. This current varies from "zero" at the ends (blue) to a maximum value somewhere else in the beam (red). Each slice is assumed to be injected into the channel with a radius and divergence which is linearly dependent on that slice's current. In this paper, the beam is assumed to be created from an idealized Pierce gun, which always provides an initial radius of 5 mm and zero divergence for the peak current slice. (b) $a_1 = b_1 = 0$, providing no variation of initial radius or divergence on slice current. (c) $a_1 = 0$, $b_1 > 0$, providing no dependence of initial radius on slice current, but some dependence of initial divergence on slice current. (d) $a_1 > 0$, $b_1 = 0$, providing some dependence of initial radius on slice current, but no dependence of initial divergence on slice current. (e) $a_1 > 0$, $b_1 > 0$, providing some dependence of both initial radius and divergence on slice current. The values of a_1 and b_1 can also be considered to define the magnitude of projected emittance in the injected beam, as described in Harris *et al.* (2013)

used, leading to unphysical negative radii. A beam energy of 10 keV, channel design radius R of 5 mm, and a peak current of 100 mA were assumed, corresponding closely to the parameters of the University of Maryland Electron Ring (Bernal et al., 2016). The envelopes of 21 slices, varying in current from 0 to 100 mA in 5 mA increments, were then calculated using a MathCAD spreadsheet over a channel length of 5 m, with 3×10^5 integration steps. This calculation was performed for a_1 values of 0, 0.01, 0.02, 0.03, 0.04, and 0.05 m/A, and for values of b_1 of 0, 0.02, 0.04, and 0.06 A^{-1}. Note that b_1 is varied less here than in Harris *et al.* (2017*b*), which reflects the recognition that large values of that parameter are generally expected to be detrimental to good transport.

Channel configurations

The channel configuration considered here involved a linear taper of the form

$$k(z) = \begin{cases} k_M + k_M \dfrac{(C-1)}{(B-A)}(z - A) & \text{for } A \le z \le B \\ C\,k_M & \text{for } \quad z > B \end{cases}, \tag{4}$$

where C is the ratio of the starting and ending focusing strength, which will be referred to as the taper strength, while $C/(B - A)$ defines the taper rate (Fig. 3). The quantity k_M is the focusing strength required for matched transport of the peak current beam in an untapered channel (7.739 m^{-1}). The taper starting position A will always be zero in the calculations discussed here but is included in Eq. (4) for completeness. Note that a linear taper in channel strength does not yield a linear taper in beam

https://doi.org/10.1017/S0263034619000612 Published online by Cambridge University Press

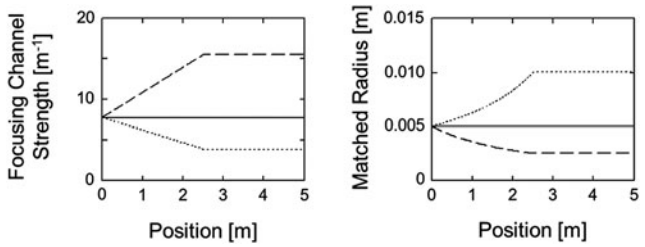

Fig. 3. Focusing channel strength [$k_m(z)$] as a function of position z downstream in the channel (left), and the resulting local matched beam radius as a function of position for a 100 mA, 10 keV electron beam (right), for the linear taper with $A = 0$ m and $B = 2.5$ m, and taper strengths C of 2 (dash), 1 (solid), and 0.5 (dotted).

radius, as the matched radius (in the limit of small emittance) varies inversely with the channel strength:

$$R_{\mathrm{m}} = \frac{\sqrt{K}}{k_0}. \tag{5}$$

Several cases of the linear tapered channel were also run with changes in beam emittance. In these cases, the matched channel strength k_{M} was not recalculated to properly match the beam with the increased emittance.

In all cases, the channel taper start A will be set to zero, the channel entrance. The parameter space to be explored will therefore consist of the following five parameters: (1) channel taper length (B); (2) channel taper strength (C); (3) degree of initial correlation between slice current and radius (a_1); (4) degree of initial correlation between slice current and divergence (b_1); and (5) slice emittance (ε).

Results matrix

For each combination of a_1 and b_1, the envelope of each of the 21 beam slices is compared to the envelope of the peak current slice to determine whether it is well confined or not, providing a "score" for that particular combination. In particular, at each of the 3×10^5 integration steps, the difference between the radius of the peak-current slice and the radius of each reduced-current slice is computed. If this difference is less than zero at any point along the 5 m focusing channel, that reduced-current slice is flagged as not well confined, and is assigned a score of zero, while if the slice is flagged as well confined, it is assigned a score of 1. These scores are summed over all of the 21 slices of the beam, forming an overall score for that particular combination of channel configuration, emittance, a_1, and b_1. For example, the simple five-slice configuration shown in Figure 1 would have a score of 4, as four of the five slices are well confined. These scores provide the values of $N_{i,j}$ used to populate a results matrix of the form

$$\begin{array}{lcccc} & b_1 = 0\,\mathrm{A}^{-1} & b_1 = 0.02\,\mathrm{A}^{-1} & b_1 = 0.04\,\mathrm{A}^{-1} & b_1 = 0.06\,\mathrm{A}^{-1} \\ a_1 = 0\,\mathrm{m/A} & N_{0,0} & N_{0,1} & N_{0,2} & N_{0,3} \\ a_1 = 0.01\,\mathrm{m/A} & N_{1,0} & N_{1,1} & N_{1,2} & N_{1,3} \\ a_1 = 0.02\,\mathrm{m/A} & N_{2,0} & N_{2,1} & N_{2,2} & N_{2,3} \\ a_1 = 0.03\,\mathrm{m/A} & N_{3,0} & N_{3,1} & N_{3,2} & N_{3,3} \\ a_1 = 0.04\,\mathrm{m/A} & N_{4,0} & N_{4,1} & N_{4,1} & N_{4,1} \\ a_1 = 0.05\,\mathrm{m/A} & N_{5,0} & N_{5,1} & N_{5,2} & N_{5,3} \end{array}, \tag{6}$$

with each channel configuration and emittance (B, C, ε) having its own results matrix. Note that the minimum value of any $N_{i,j}$ is 1, as the peak-current slice is, by definition, well confined, while the maximum is 21.

These results can be presented in several ways. First, all the elements of the matrix can be summed to provide a single, overall effectiveness score for the transport channel, with higher scores indicating improved transport of beams with initial transverse–longitudinal correlation. This overall score will be referred to as the "matrix sum"; this sum will range from a minimum of 24 to a maximum of 504.

A second approach is to sum over the elements in each of the columns, providing four effectiveness scores for each channel configuration. This can be used to study how the effectiveness of the channel improves or degrades as the value of b_1 (initial correlation between slice divergence and current) is changed. This score will be referred to as the "column sum"; this sum will range from a minimum of 6 to a maximum of 126.

A third approach is to sum over the elements in each of the rows, providing six effectiveness scores for each channel configuration. This can be used to study how the effectiveness of the channel improves or degrades as the value of a_1 (initial correlation between slice radius and current) is changed. This score will be referred to as the "row sum"; this sum will range from a minimum of 4 to a maximum of 84.

For each channel configuration, we will present these scores as a function of channel taper strength C and taper length B, in some cases, slice emittance ε.

Motivations and limitations

This approach incorporates several attempts to increase the speed of calculation and simplify the presentation of the resulting data compared to that used in Harris et al. (2017*b*). First, we have reduced the number of values of a_1 and b_1 that are used: here we use a 6×4 matrix, while in Harris et al. (2017*b*), we used a 26×21 matrix. Second, for every value of (a_1,b_1), we calculate 21 slices of varying current here, while in Harris et al. (2017*b*), we calculated 101 slices. Third, we are presenting matrix, column, or row sums rather than presenting the entire results matrix. This loses the granularity of the previous presentation but enables presentation of results from a much larger set of test configurations to aid in recognizing trends in the data. Understanding these trends is our primary objective, rather than a detailed analysis of any given configuration, for which more sophisticated techniques such as particle-in-cell codes, which incorporate more physics, are better suited.

Because it relies on the transverse envelope equation, our approach necessarily leaves out a large number of potentially interesting effects. Most importantly, as discussed above, it does not incorporate longitudinal evolution of the beam. Similarly, it

https://doi.org/10.1017/S0263034619000612 Published online by Cambridge University Press

assumes no transverse variation in current across the beam, which can occur due to variations in cathode temperature, variations in electric field due to cathode edge effects (Umstattd and Luginsland, 2001), and control grid effects (Spangenberg, 1948), due to changes in cathode properties over time (Harris et al., 2017*a*), or through beam-dynamical effects (Bernal et al., 1999*b*). It also does not take into account nonlinear focusing and the resulting aberrations which are known to be produced by solenoid magnets (Biswas, 2013; Lund, 2015). We also assume a direct injection of the beam into the entrance of the solenoid channel, implicitly assuming a hard-edge solenoid model at the upstream end which is known to introduce issues (Biswas, 2013) and is unrealistic for most practical purposes. The latter assumption was incorporated to further reduce the complexity of the problem. Additionally, our objective here was not to optimize the transport of beams with varying initial conditions in tapered transport channels, but rather as a simple model for exploring the consequences of initial transverse–longitudinal correlations in intense beams.

Additionally, our assumption of zero divergence injection of the peak current slice and our definition of "well-confined" transport as being relative to the envelope of the peak-current slice are not the only possible choices, and other choices may be more appropriate in certain circumstances. For example, if a beam were required to pass through a particular beam tunnel of known radius, that radius would be a more appropriate reference standard. In other cases, a composite reference radius could be produced by taking the largest radius at each location of (for example) the five slices with the highest current. The general approach used here, then, can be tailored to focus on different aspects of the problem which are most important in any given case.

Results

Linear taper with fixed emittance

Figure 4 shows an example of the beam envelopes calculated for a tapered channel of taper length 2.5 m and taper strength 2, for three combinations of a_1 and b_1. This figure emphasizes the role played by reducing the initial radii of slices with lower slice currents. As they are injected initially closer to their matched radii, the amount of radial kinetic energy carried by these slices is lower, resulting in lower mismatch amplitudes, which are therefore less likely to exceed the radius of the peak current slice.

Figure 5 shows the matrix sum as a function of the taper strength C, for several values of taper length B; in this figure, data from each value of B is shown in a different color. As mentioned above, the matrix sum is equal to the total number of well-confined slices summed over all combinations of (a_1, b_1) and has a maximum value of 504 (=21 values of current × 6 values of a_1 × 4 values of b_1). The 1 μm emittance was not sufficient to ensure proper transport of the zero current slices at the maximum value of a_1 (which would start the zero current slice with an unrealistic radius of zero and, for $b_1 > 0$, with a negative divergence), and so, the maximum value actually attained was 500. The taper begins at zero ($A = 0$ m) in all cases. As the taper is made more abrupt (smaller B), performance generally worsens. From $C = 0.1$ to 0.9, the matrix sum is maximized for the more gentle tapers, and degraded performance is seen for the more abrupt tapers, with the worst performance occurring around $C = 0.5$. From approximately $C = 0.9$ to 1.1, qualitatively similar

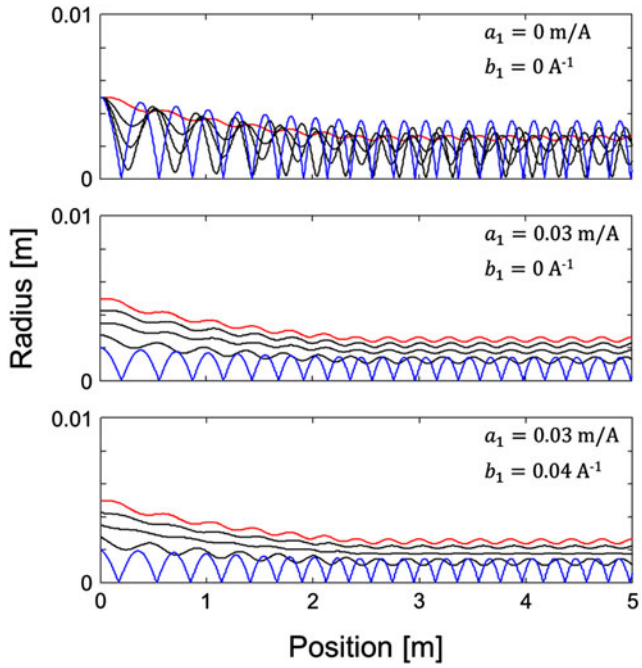

Fig. 4. Example of beam transport in a tapered channel. Beam envelopes for 10 keV electron beams injected with currents of 100 mA (red); 75, 50, and 25 mA (black); and 0 mA (blue) into a linearly tapered solenoidal focusing channel with parameters $A = 0$ m, $B = 2.5$ m, and $C = 2$. The beam slices are injected with initial correlations between slice current, radius, and divergence of (0 m/A, 0 A^{-1}) (top), (0.03 m/A, 0 A^{-1}) (middle), and (0.03 m/A, 0.04 A^{-1}) (bottom). The cases with increased initial correlation between slice radius and slice current have much-improved transport and are well confined over the 5 m channel length.

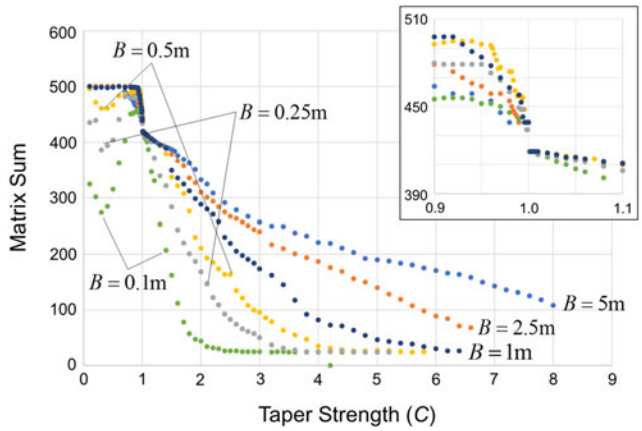

Fig. 5. Linear taper results. Matrix sum as a function of taper strength (C) for several values of taper length (B).

performance exists for all taper lengths, with performance decreasing rapidly as $C = 1$ is approached from below, and then more slowly after that. This region is detailed in the inset. Above approximately $C = 1.1$, performance continues to decrease, with faster decreases for faster ramp rates $C/(B - A)$.

Figure 6 shows the column sums as a function of taper strength C, for the various values of taper length B; in this figure, the data point colors correspond to the different values of b_1, as indicated at the top of the figure. As discussed above, taking the column sums from Eq. (6) is a way of assessing the effect of changing b_1, the strength of correlation between slice current

https://doi.org/10.1017/S0263034619000612 Published online by Cambridge University Press

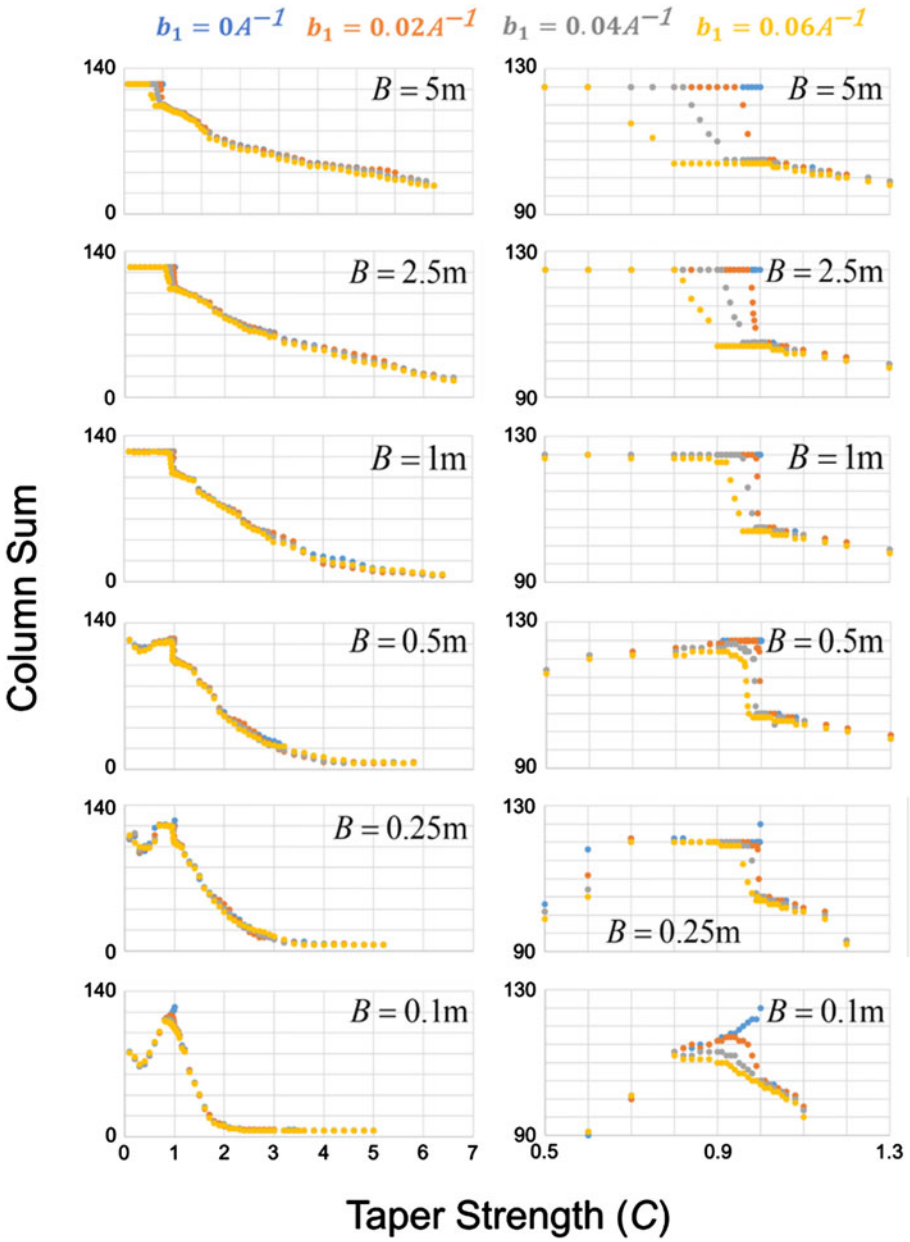

Fig. 6. Linear taper results. Column sum as a function of taper strength (C) for several values of taper length (B) and initial divergence–current correlation (b_1). The maximum indicated value of the column sum is 125, slightly less than the theoretical maximum value of 126 (21 values of current × 6 values of a_1). This difference is due to incorrect handling of the zero current slice in the $a_1 = 0.05$ m/A case, as discussed in the text.

and initial slice divergence on entering the channel. In general, the value of b_1 had little effect on the number of well-confined slices transported through the channel. The primary exceptions to this occurred in the transition region about $C = 1$, where performance improved for smaller values of b_1. This improvement was generally larger for the most gentle tapers, although a qualitatively distinct behavior emerges at $B = 0.1$ m, which again favors smaller values of b_1. In all cases, $C = 1$ and $b_1 = 0$ A^{-1} provide the maximum number of well-confined slices, and there is an abrupt transition once $C > 1$.

This abrupt transition can be explained as follows. For $C = 1$, the channel is simply a uniform focusing channel, so changes in the value of B do not affect system performance. With $b_1 = 0$ A^{-1}, the initial divergence of each slice is zero, so we need only consider the radial potential energy associated with each slice's initial radius. For the case of $a_1 = 0$ m/A, each slice is injected at the same radius, which will be its maximum radius, and therefore no slice will exceed the radius of the peak current slice (Fig. 7, top). For larger values of a_1, the reduced-current slices are injected at smaller initial radii and may expand somewhat, but not enough to exceed the peak current slice (Fig. 7, middle). Increasing the channel taper slightly now to $C = 1.001$, we find similar results, except that all of the reduced-current slices for $a_1 = 0$ m/A are no longer well confined, which is the cause of the sudden drop at $C = 1$ shown in Figure 6. This is only evident in the envelope figures by zooming in closely, so that the very small excursions of the reduced-current slice radii beyond that of the peak current slice are apparent (Fig. 7, bottom).

The other interesting area is the notch that forms for values of C around 0.5. To investigate this, we considered the $b_1 = 0$ A^{-1}, $C = 0.5$ cases for $B = 5$ and 0.1 m. In the former case, all slices except the zero current slice for $a_1 = 0$ m/A were well confined. In the latter case, all slices for $a_1 = 0.02$, 0.03, and 0.04 m/A were well confined, while all slices (except the peak current

https://doi.org/10.1017/S0263034619000612 Published online by Cambridge University Press

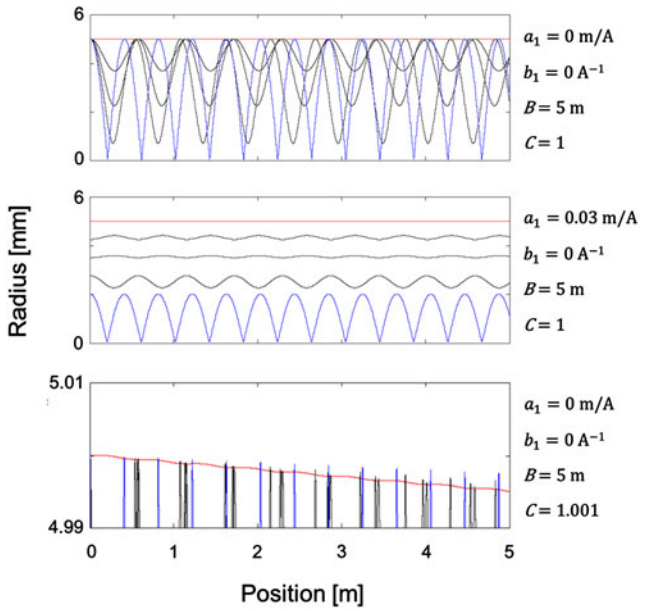

Fig. 7. Slice envelopes for three transport conditions near $C = 1$.

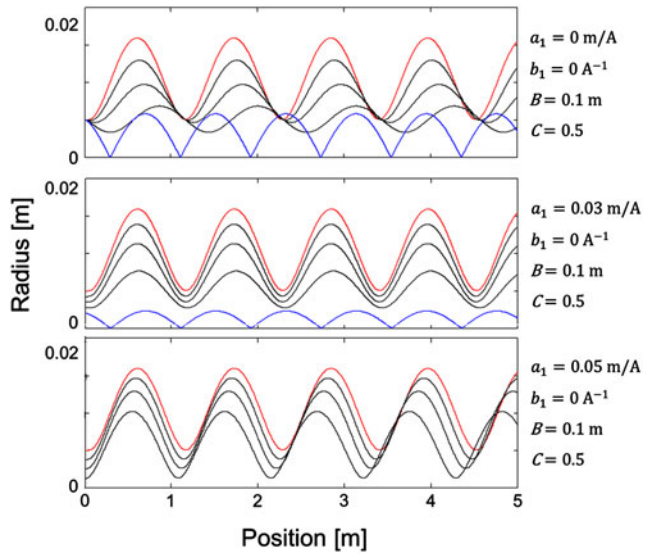

Fig. 8. Slice envelopes for three transport conditions near $C = 0.5$.

slice) for $a_1 = 0.05$ m/A were not well confined, all the slices between 40 and 85 mA were not well confined for $a_1 = 0.01$ m/A, and all slices but 5, 10, 15, and 100 mA are not well confined for $a_1 = 0$ m/A. This suggests a preference for a_1 values around 0.03 m/A, which we will see again later. It also indicates that in this region, higher currents are more susceptible to being not well confined. In the case of $B = 5$ m, the peak current slice increases in radius gradually without noticeable high-spatial frequency mismatch oscillations, while the reduced current slices do undergo high-spatial frequency mismatch oscillations but do not exceed the radius of the peak current slice. In the case of $B = 0.1$ m (Fig. 8, top), both the peak and reduced-current slices undergo high-spatial frequency mismatch oscillations which tend to dephase over time, such that the reduced current slices become not well confined at the locations of the peak current slice waists. For values of a_1 near 0.03 m/A, the mismatch oscillations are initially more closely in phase, requiring the beam to travel longer distances before their dephasing leads to the onset of non well-confined behavior, and those distances are larger than the 5 m channel length considered here (Fig. 8, middle). For lower values of a_1, the peaks of the reduced current slice mismatch oscillations gradually slip ahead of those of the peak current slice (Fig. 8, top), while in the case of higher values of a_1, they gradually slip backwards (Fig. 8, bottom). For values of a_1 near 0.03 m/A, the phase slip is minimized for the higher current slices, while the lower current slices' radii are lower than the peak current slice's waist radii preventing a non well-confined scenario.

Figure 9 shows the row sums from Eq. (6), as a function of taper strength C, for various values of B; in this figure, the data point colors correspond to different values of a_1, as indicated in the right of the figure. Taking the row sums from Eq. (6) is a way of assessing the effect of changing a_1, the strength of correlation between slice current and initial slice radius on entering the channel. Unlike b_1, there is an overall pronounced improvement from choosing the correct value of a_1, with dramatically improved performance obtained from using a_1 values between 0.02 and 0.04 m/A. This improvement was most pronounced in the case of the longer tapers. In almost every case, the worst performance was achieved from using a value of 0 m/A, in which no correlation was assumed.

These results are consistent with observations from previous work that properly constructed initial transverse–longitudinal correlations aid in beam transport, with some initial correlation between slice current and radius being desired, but with correlation between slice current and divergence generally being detrimental.

Linear taper with emittance varied

A question raised by the peer reviewers of Harris *et al.* (2017*b*) was, what would be the impact of changes in beam emittance on transport through the focusing channel? To consider this in the context of the linearly tapered channel, six sets of calculations were performed. Linear tapers of length 5 and 0.1 m were used, with the taper strength C varied as before. For each of these taper lengths, three values of slice emittance were used: 1, 5, and 10 μm. No change in the channel strength was made to account for these higher emittances. The results are shown in Figures 10–12, where the data point color refers to slice emittance and the data point shape refers to taper length B, as indicated to the right of each figure.

Figure 10 shows the matrix sum for the calculated cases, with taper lengths B of 5 m denoted by solid circles and 0.1 m denoted by hollow squares, and with slice emittances of 1, 5, and 10 μm shown with blue, red, and black, respectively. The general behavior of the $B = 5$ and $B = 0.1$ m cases are as shown previously. There is some dependence on slice emittance, which is generally relatively weak except for the longer taper at larger values of taper strength.

Figure 11 shows the data broken out by different values of b_1. The general trends are exactly as shown in Figure 10, with higher values of emittance providing slightly worse transport, and with this effect being most pronounced for the long, 5 m taper at large values of taper strength.

Figure 12 shows the data broken out by different values of a_1. Here, we see several very clear trends. First, the long taper again

https://doi.org/10.1017/S0263034619000612 Published online by Cambridge University Press

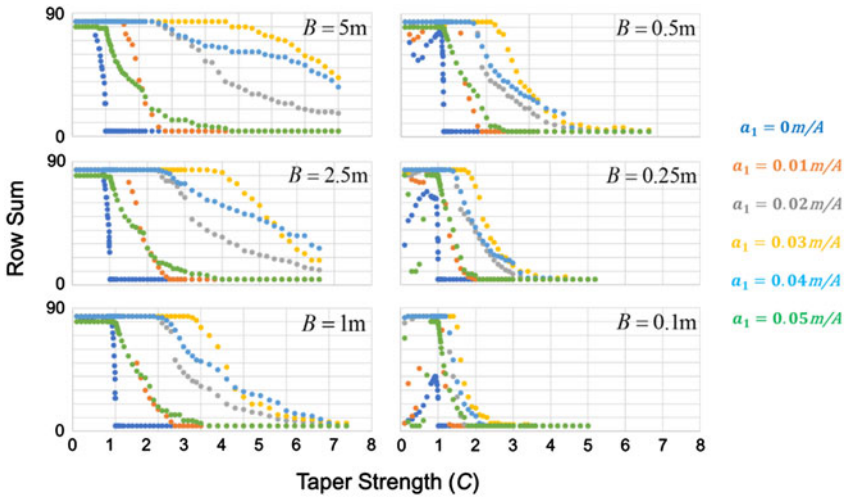

Fig. 9. Linear taper results. Row sum as a function of taper strength (C) for several values of taper length (B) and initial radius–current correlation (a_1). Values of 0.03 and 0.04 m/A are preferred over the entire range of channel taper values C, with 0.03 m/A generally being preferred but with 0.04 m/A being preferred for intermediate values of B at very high values of C.

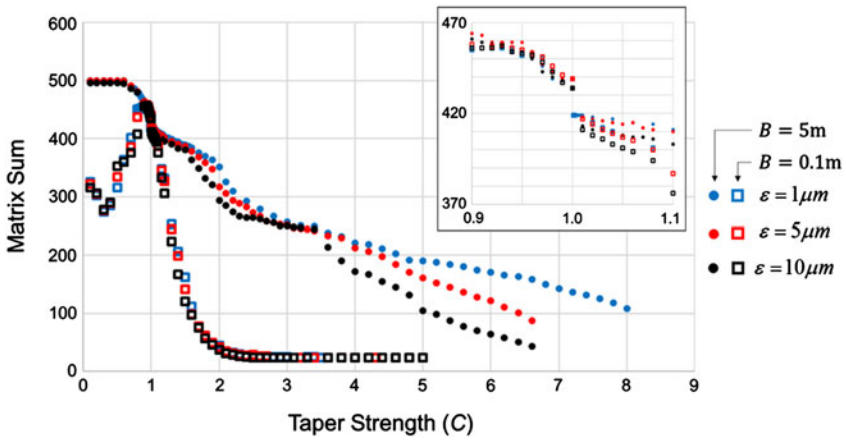

Fig. 10. Effect of beam emittance. Matrix sum as a function of linear taper strength C for taper lengths B of 5 m (solid circles) and 0.1 m (hollow squares), for slice emittances of 1 μm (blue), 5 μm (red), and 10 μm (black).

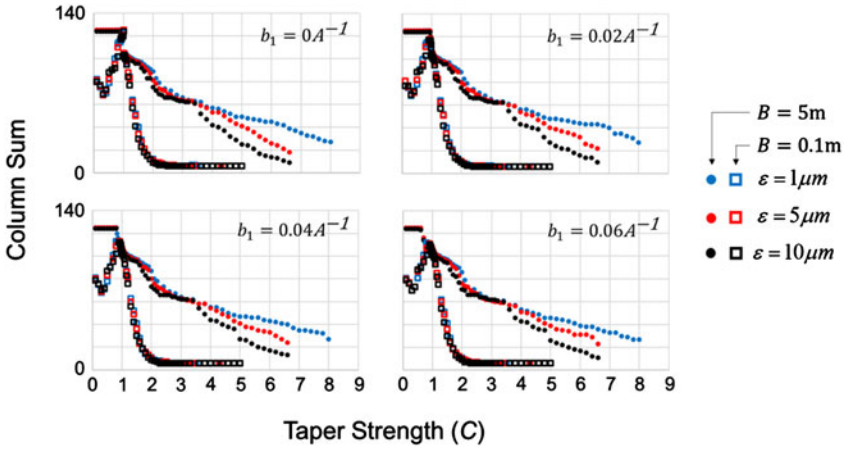

Fig. 11. Effect of beam emittance. Each panel shows the column sum from Eq. (6) corresponding to a single value of b_1.

provides generally better transport over a wider range of taper strengths (C) than does the short taper. We again see that as the value of a_1 is increased, good transport occurs over a wider range of taper strengths, with best transport occurring around $a_1 = 0.03$ m/A. Continuing to increase a_1 beyond that point causes the beam transport to degrade. This behavior is most pronounced in the long taper but is also present on the short taper. For the long taper, there is also a clear difference in transport effectiveness which depends on emittance, with improved transport generally occurring with lower emittance, and with the effect of emittance on the transport being maximized near $a_1 = 0.03$ m/A.

Surprisingly, for $a_1 = 0.04$ m/A, for taper strengths between about 2.5 and 5, higher slice emittance actually provides *improved* transport in the long taper case. This implies that optimal

https://doi.org/10.1017/S0263034619000612 Published online by Cambridge University Press

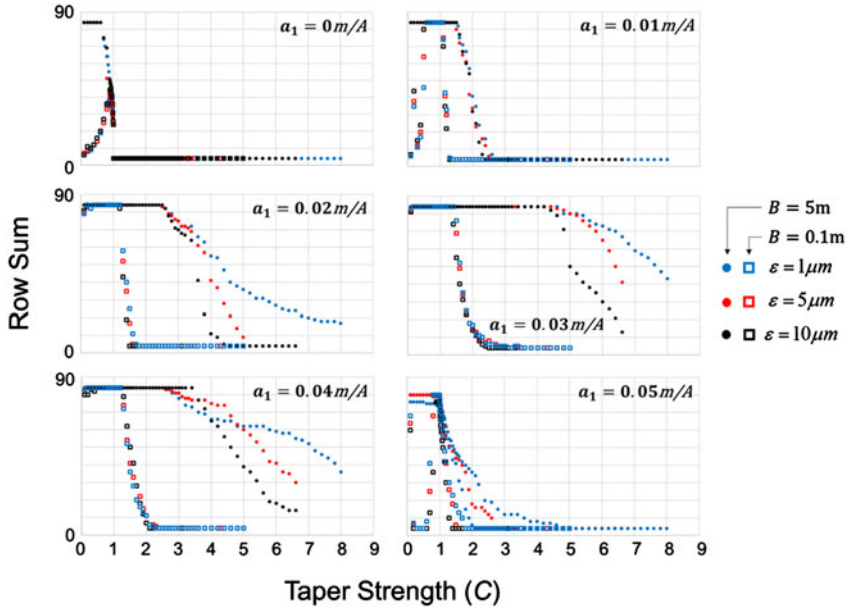

Fig. 12. Effect of beam emittance. Each panel shows the row sum from Eq. (6) corresponding to a single value of a_1.

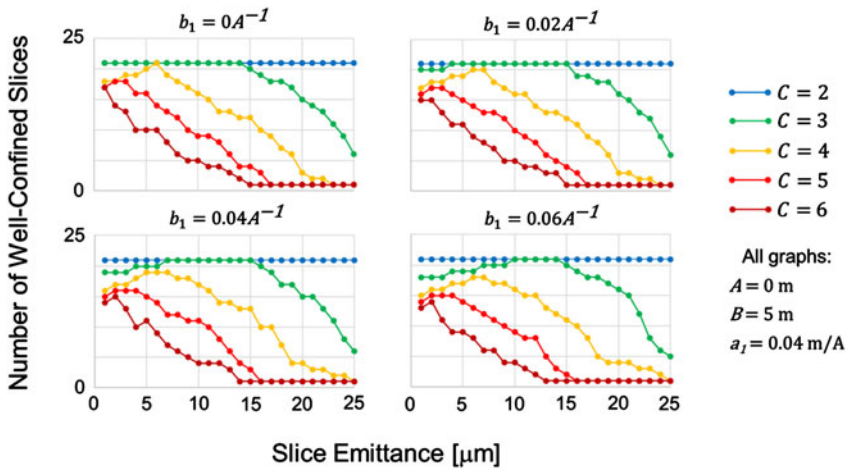

Fig. 13. Number of well-confined slices as a function of slice emittance and taper strength for the long linearly tapered channel, with $a_1 = 0.04$ m/A.

performance, per our definition of well-confined transport, requires not only the proper settings of a_1 and b_1 but also the proper value of slice emittance.

To investigate this further, we will consider how the number of well-confined slices varies as the slice emittance is changed from 1 to 25 μm in the long linear taper case ($B = 5$ m) with $a_1 = 0.04$ m/A, and how this depends on values of b_1. Figure 13 shows four panels, each of which corresponds to a single value of b_1. In each panel, several sets of data are plotted, which correspond to different values of the taper strength C. These show that, particularly for taper strengths of 3–5, the number of well-confined slices is maximized when the emittance is slightly higher than 1 μm, and that the prominence of this effect increases as b_1 increases.

A particularly strong effect was evident in the $b_1 = 0.04$ A^{-1}, $C = 4$ case. Figure 14 shows the behavior in this case for each of the 21 slice currents, on the vertical scale, as the slice emittance is increased from 1 to 25 μm, on the horizontal scale. Slices which are well confined for a given slice emittance are indicated in green while slices which are not well confined for a given slice emittance are indicated in red. The existence of an optimal

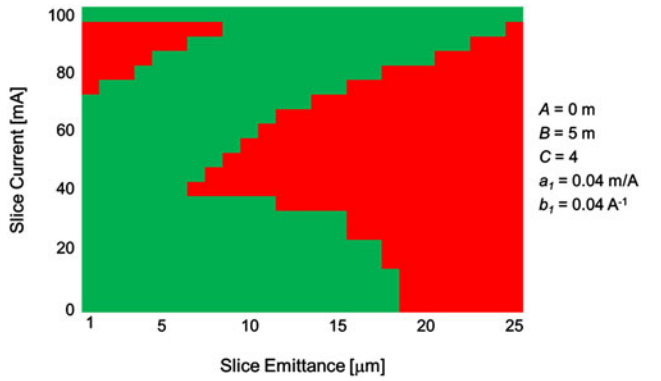

Fig. 14. Impact of slice current and slice emittance on transport effectiveness for the conditions indicated at right. Green indicates well-confined transport, while red indicates non-well-confined transport.

value of slice emittance is evidently due to the competing impacts of an initial improving transport of high-current slices at low values of emittance and an increasingly poor transport beginning in

https://doi.org/10.1017/S0263034619000612 Published online by Cambridge University Press

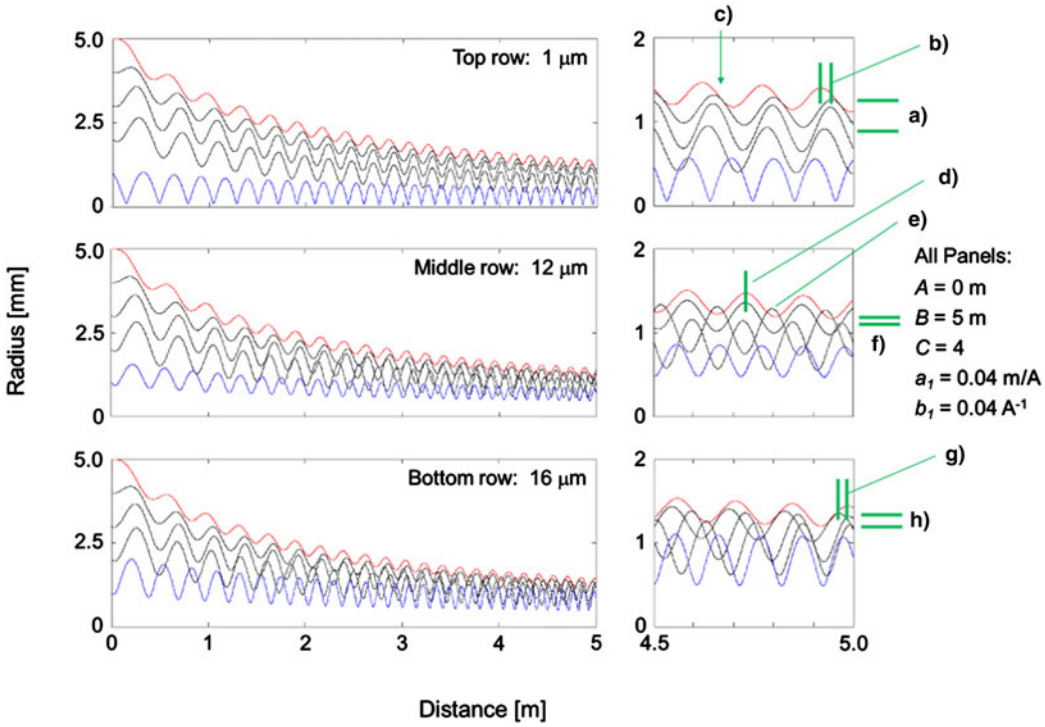

Fig. 15. Impact of slice current and slice emittance on transport effectiveness for the conditions indicated at right. (a) Average radius of lower-current slices is generally significantly less than that of the peak-current slice in the 1 μm case. (b) This is not true for the 75 mA, and other higher current slices, whose mismatch oscillations are out of phase with that of the peak current slice. (c) These facts combine to enable non well-confined transport for the higher current slices at 1 mm, although the excursions beyond the peak current slice radius are very small. (d) When the emittance is increased to 12 μm, the higher current slices are now more closely in phase with the peak current slice, reducing the opportunity for non well-confined transport, and accounting for the initial improvement in transport indicated in Figure 14 as emittance is increased. (e) Increasing emittance has also caused the mid-current slices to both shift phase and to increase their average radii, causing them to become non well confined. (f) At 12 μm, the lower current slices still have radii which are smaller than the waists of the peak current slice, so their transport is initially still well confined. (g) Moving to still higher emittances, the higher current slices have now continued their phase shifting relative to the peak current slice, to the point where they are beginning to experience non well-confined transport. (h) Increasing values of emittance also now lead to larger average radii for the lower-current slices, opening the opportunity for non well-confined transport with them as well.

the 40 mA slice and spreading from there towards both the high-current and low-current slices as emittance passes 7 μm.

This can also be seen from the envelopes for various slices as shown in Figure 15. Increasing slice emittance increases the average radius of all slices at the end of the channel, but this effect is stronger for smaller slice currents. At 1 μm emittance, the lower-current slice radii are generally well below that of the peak current slice (a). An exception is the 75 mA slice, which has a somewhat smaller average radius, but whose mismatch oscillations are out of phase with those of the peak current slice (b), leading to a non-well-confined condition at the end of the channel (c). As the emittance increases to 12 μm, the local maximum radii at the end of the channel for the 75 mA slice are closer to those of the peak current slice, but this is compensated for because the two slices' mismatch oscillations, which are initially out of phase, come approximately into phase by the end of the channel (d). This improves transport for the 75 mA, and other high-current slices, as defined by our metric. Continuing to increase the slice emittance, as shown with the envelopes for 16 μm, follows through with this phase-slippage process for the high-current slices, such that they are now beginning to slip out of phase with respect to the peak current slice (g). Meanwhile, the relatively greater effect of increased emittance on the lower-current slices has caused their local maximum radii for more of these slices to exceed the local minimum radius of the peak current slice (h), thus increasing the number of relatively lower current slices which become non-well-confined.

The optimal value of emittance is therefore seen to be due to the combined effects of the relatively stronger impact on lower-current slices from increasing slice emittance, and from the emittance-driven changes in mismatch period, particularly for the higher current slices.

Summary

Here we considered the transport of space charge-dominated electron beams through tapered solenoid channels having linear dependences of the focusing strength on axial position. The beams were assumed to be created from an idealized Pierce-type gun providing a beam with zero initial divergence at full current, and otherwise having a linear dependence of the initial slice divergence and radius on the slice current. No longitudinal evolution of the beam was incorporated. A slice emittance of 1 μm was used in most cases, but the effect of slice emittance on transport effectiveness was also investigated. A total of 21 beam slices with currents varying from 0 to 100 mA were considered, and the transport effectiveness was quantified by the number of slices whose radii were always less than or equal to that of the 100 mA slice. Longer taper lengths generally provided improved transport, as did minimizing the initial correlation between slice divergence and slice current, and providing a moderate degree

https://doi.org/10.1017/S0263034619000612 Published online by Cambridge University Press

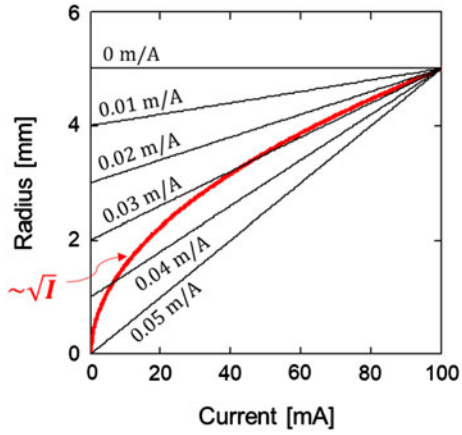

Fig. 16. Comparison of linear and ellipsoidal correlations between slice current and slice radius for different values of a_1, according to Eq. (1). Note that values of 0.03 m/A generally provide the best match between the linear model and the ellipsoidal model, but under more extreme values of reduced current, values closer to 0.04 m/A may be preferred. This mirrors the results of row sum calculations where 0.03 m/A is generally preferred but in extreme cases, 0.04 m/A is preferred. Note also the greatly improved performance in Figure 8 for $a_1 = 0.03$ m/A.

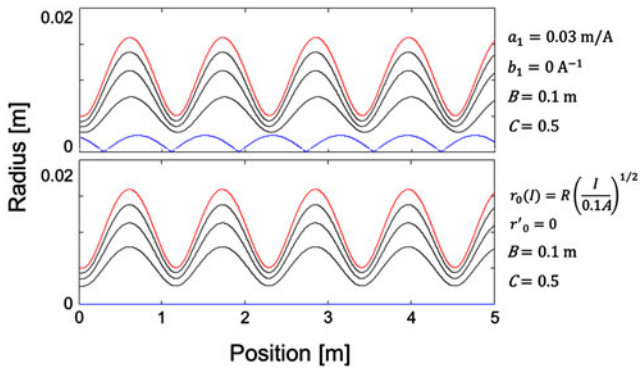

Fig. 17. (Top) Beam envelopes for 100 mA (red); 75 mA, 50 mA, and 25 mA (black); and 25 mA (blue) slices; for the indicated conditions, as shown previously in Figure 8. (Bottom) The same envelopes, but now assuming injection of a beam with $r \sim \sqrt{I}, r' = 0$, and with zero emittance. With emittance increased to 1 μm, this panel looks identical except that very small currents approaching zero become non-physical due to their being injected with a theoretical radius of zero which yields an infinite emittance-driven impulse. This emphasizes the similarity of $a_1 = 0.03$ m/A to the ideal case for transport.

of initial correlation between initial slice radius and slice current. The latter two dependences are consistent with our previous studies of transport in other channel configurations and therefore appear to be widely applicable. Lower slice emittances were also generally preferred, with the dependence on slice emittance being largest for long, strong tapers and degrees of transverse–longitudinal correlation which optimized beam transport. Unexpectedly, the transport was actually *improved* by slightly larger values of slice emittance under certain limited conditions. Finally, we note that the optimum values of a_1 were found to be around 0.03 m/A. Of the tested values of a_1, this most closely approximates a scaling of $r(I) \sim \sqrt{I}$(Fig. 16), which, if fully met could enable simultaneous matched transport for all slices in the beam (Fig. 17) and is a feature of the highly sought 3D ellipsoidal beam distribution (Li and Lewellen, 2008; Limborg-Deprey and Bolton, 2006).

References

Bernal S, Kishek RA, Reiser M and Haber I (1999*a*) Observations and simulations of particle-density oscillations in an apertured, space-charge dominated electron beam. *Proceedings of the 1999 Particle Accelerator Conference (Cat. No. 99CH36366)*, 1749–1751. New York: IEEE.

Bernal S, Kishek RA, Reiser M and Haber I (1999*b*) Observations and simulations of transverse density waves in a collimated space-charge dominated electron beam. *Physical Review Letters* **82**, 4002.

Bernal S, Quinn B, Reiser M and O'Shea PG (2002) Edge imaging in intense beams. *Physical Review Special Topics – Accelerators and Beams* **5**, 064202.

Bernal S, Li H, Kishek RA, Quinn B, Walter M, Reiser M, O'Shea PG and Allen CK (2006) RMS envelope matching of electron beams from "zero" current to extreme space charge in a fixed lattice of short magnets. *Physical Review Special Topics – Accelerators and Beams* **9**, 064202.

Bernal S, Beaudoin B, Haber I, Koeth T, Mo Y, Montgomery E, Rezaei KP, Ruisard K, Stern W, Sutter D, Zang H and Kishek RA (2016) Nonlinear dynamics with space-charge in a small electron recirculator. *AIP Conference Proceedings* 1777, 100003.

Biswas B (2013) A model of field and spherical aberration in soft/hard edge solenoid magnets. *Review of Scientific Instruments* **84**, 103301.

Brinkmann R, Derbenev Y and Flottmann K (2001) A low emittance, flat-beam electron source for linear colliders. *Physical Review Special Topics – Accelerators and Beams* **4**, 053501.

Efthymiopoulos L, Gilardoni S, Hansen OM and Prior G (2013) A simplified magnetic field tapering and target optimisation for the neutrino factory capture system. *Proceedings of the 2013 International Particle Accelerator Conference*, 1370–1372. Available at: https://accelconf.web.cern.ch/accelconf/IPAC2013/papers/tupfi018.pdf

Ein-Gal M (2009) Adjustable aperture collimator. U.S. Patent 7,489,764, February 10.

Floettmann K (2004) Positron source options for linear colliders. *Proceedings of the 2004 European Particle Accelerator Conference*, 69–73. Available at: https://accelconf.web.cern.ch/accelconf/e04/PAPERS/TUZACH01.PDF

Harris JR and Lewellen JW (2010*a*) Transmission of intense electron beams through apertures. *Physics of Plasmas* **17**, 043101.

Harris JR and Lewellen JW (2010*b*) Suppression of current fluctuations in an intense electron beam. *Journal of Applied Physics* **108**, 083301.

Harris JR, Feldman RB and O'Shea PG (2007*a*) Transverse-longitudinal coupling in an intense electron beam. *Proceedings of the 2007 Particle Accelerator Conference*, 3597–3599. New York: IEEE.

Harris JR, Neumann JG, Tian K and O'Shea PG (2007*b*) Longitudinal density modulation and energy conversion in intense beams. *Physical Review E* **76**, 026402.

Harris JR, Lewellen JW and Poole BR (2012) Transverse-longitudinal correlations in electron guns. *Journal of Applied Physics* **112**, 023304.

Harris JR, Lewellen JW and Poole BR (2013) Transport of electron beams with initial transverse-longitudinal correlation. *Journal of Applied Physics* **114**, 063304.

Harris JR, Jensen KL, Maestas S, Tang W and Shiffler DA (2017*a*) Practical considerations in the modeling of field emitter arrays with line charge distributions. *Journal of Applied Physics* **121**, 203303.

Harris JR, Poole BR and Lewellen JW (2017*b*) Solenoid transport of beams with current-dependent initial conditions. *Journal of Applied Physics* **122**, 093302.

Hoff BW, French D.M, Simon DS, Lepell PD, Montoya T and Heidger SL (2017) High current nonlinear transmission line based electron beam driver. *Physical Review Accelerators and Beams* **20**, 100401.

James MB, Donahue RJ, Miller RH and Nelson WR (1991) A new target design and capture strategy for high-yield positron production in electron linear colliders. *Nuclear Instruments and Methods A* **307**, 207–212.

Leupold HA (1987) Leakage-free, linearly varying axial permanent magnet field source. U.S. Patent 4,701,737, October 20.

Leupold HA (1993) Magnetic field sources for producing high-intensity variable fields. U.S. Patent 5,216,400, June 1.

Leupold HA, Tilak AS and Potenziani E (1992) Tapered fields in cylindrical and spherical spaces. IEEE Transactions on Magnetics **28**, 3045–3047.

https://doi.org/10.1017/S0263034619000612 Published online by Cambridge University Press

Li Y and Lewellen JW (2008) Generating a quasiellipsoidal electron beam by 3D laser-pulse shaping. *Physical Review Letters* **100**, 074801.

Limborg-Deprey C and Bolton PR (2006) Optimum electron distributions for space charge dominated beams in photoinjectors. *Nuclear Instruments and Methods in Physics A* **557**, 106–116.

Lund SM (2015) Nonlinear optics of solenoid magnets. Proceedings of the 2015 International Particle Accelerator Conference, 4048–4050. Available at: http://accelconf.web.cern.ch/AccelConf/IPAC2015/papers/thpf139.pdf.

McDonald KT, Sayed HK, Berg JS, Kirk HG and Palmer RB (2014) Optimized capture-solenoid field for a muon accelerator font end. Available at: http://cosmology.princeton.edu/mumu/target/Sayed/140129/SolTaper-140129_k9.pdf

Mohsen O, Gonin I, Kephart R, Khabiboulline T, Piot P, Solyak N, Thangaraj JC and Yakovlev V (2018) Initial beam dynamics simulations of a high-average-current field-emission electron source in a superconducting radiofrequency gun. *Nuclear Instruments and Methods A* **909**, 456–459.

Peterson RE (2011) *Shielding Requirements for an Energy-Recovery Linac Free-Electron Laser*. MS Thesis, Naval Postgraduate School.

Pierce JR (1940) Rectilinear electron flow in beams. *Journal of Applied Physics* **11**, 548–554.

Poole BR, Blackfield DT, Chen Y-J, Harris JR and O'Shea PG (2009) Space charge waves in mismatched beams. *Proceedings of the 2009 Particle Accelerator Conference*, 3272–3274. Available at: https://accelconf.web.cern.ch/AccelConf/PAC2009/papers/th5pfp035.pdf

Poursaleh A (2013) Design and simulation of high power RF modulated triode electron gun. *Life Science Journal* **10**, 2685–2689.

Reiser M (2008) *Theory and Design of Charged Particle Beams*. New York: Wiley.

Sayed HK and Berg JS (2014) Optimized capture section for a muon accelerator front end. *Physical Review Special Topics – Accelerators and Beams* **17**, 070102.

Spangenberg KR (1948) *Vacuum Tubes*. McGraw-Hill: New York.

Stancari G, Valishev A, Annala G, Kuznetsov G, Shiltsev V, Still DA and Vorobiev LG. (2011) Collimation with hollow electron beams. *Physical Review Letters* **107**, 084802.

Umstattd RJ and Luginsland JW (2001) Two-dimensional space-charge-limited emission: beam-edge characteristics and applications. *Physical Review Letters* **87**, 145002.

https://doi.org/10.1017/S0263034619000612 Published online by Cambridge University Press